Central European Geology, Vol. 60/2, 173–200 (2017)
DOI: 10.1556/24.60.2017.007
First published online September 12, 2017

Shock-induced alterations in the recently found H chondrite Csátalja meteorite and its implications

Ildikó Gyollai[1,2]*, Ákos Kereszturi[1], Zsolt Kereszty[3], Máté Szabó[4], Elias Chatzitheodoridis[5]

[1]Astrophysical and Geochemical Laboratory, Konkoly Thege Miklós Astronomical Institute, Research Centre for Astronomy and Earth Sciences, Budapest, Hungary
[2]Geobiomineralization and Astrobiological Research Group, Institute of Geological and Geochemical Research, Research Centre for Astronomy and Earth Sciences, Budapest, Hungary
[3]International Meteorite Collectors Association and Meteoritical Society, Gyor, Hungary
[4]Archemometrical Research Group, Institute of Geological and Geochemical Research, Research Centre for Astronomy and Earth Sciences, Budapest, Hungary
[5]Department of Geological Sciences, School of Mining and Metallurgical Engineering, National Technical University of Athens, Athens, Greece

Received: October 7, 2016; accepted: July 3, 2017

Shock-driven annealing of pyroxene and shock deformation of olivine were analyzed in a recently found H chondrite called Csátalja. The most characteristic infrared (IR) spectral shape of shock-annealed sub-grained pyroxene was identified: the strongest peak occurs at 860 cm^{-1} with a smaller shoulder at 837−840 cm^{-1}, and small bands are at 686, 635−638, and 1,044−1,050 cm^{-1}. The appearance of forbidden bands in pyroxene and shift of band positions to a lower wave number in olivines clearly demonstrate the crystal lattice disordering due to shock metamorphism. The shock annealing produced mixed dark melt along fractures, which consists of feldspar−pyroxene and olivine−pyroxene melt. The dark shock melt at sub-grain boundaries of shocked pyroxenes and along fracture of pyroxenes is characterized by elevated Ca, Na, and Al content relative to its environment, detected by element mapping. So far, shock deformation of pyroxene and olivine was not studied by IR spectroscopy; this method has turned out to be a powerful tool in identifying the mixed composition of shock melt minerals. Further study of shock annealing of minerals, together with the context of shock melting at sub-grain boundaries, will provide a better understanding of the formation of high P–T minerals.

Keywords: Csátalja meteorite, H chondrite, shock metamorphism, shock annealing, thermal metamorphism, element mapping, infrared spectrometry

*Corresponding author: Ildikó Gyollai; Astrophysical and Geochemical Laboratory, Konkoly Thege Miklós Astronomical Institute, Research Centre for Astronomy and Earth Sciences, Konkoly Thege Miklós út 15−17, Budapest H-1121, Hungary
E-mail: gyildi@gmail.com

ISSN 1788-2281

Introduction

Shock alterations play an important role in many meteorites (Lange et al. 1985; Keil et al. 1992; Friedrich et al. 2004; Rubin and Bottke 2009; Krzesińska and Fritz 2014) and help reconstruct the geologic history of a given specimen and also its parent body (Przylibski et al. 2003). In this study, we analyzed the shock-driven alteration of a recently found Hungarian meteorite called Csátalja (Kovács et al. 2015b) to understand the style and products of its shock alteration. In addition, we extrapolate using these results to understand and interpret similar alterations in other chondrites. The specific aims of this research are: (1) to better understand the shock-driven alteration in pyroxenes (and other minerals for context) including spatial characteristics and (2) to provide infrared (IR) spectroscopy-based information on these alterations to use them as references for the interpretation of shock-driven alterations in other meteorites in the future.

Csátalja is an H chondrite, which is among the most frequently found meteorites. They have high iron (Fe) abundance (25–31 wt%); their main minerals are orthopyroxene and olivine. Their fayalite content is usually between 16 and 20 mol% and they contain 15%–19% reduced Ni–Fe metal and 5% troilite (Bérczi 2000; Bérczi et al. 2004). These minerals are partly metamorphosed to various petrographic grades, usually between 3 and 7 (Van Schmus and Wood 1967), but 5 on average. Their trace element and oxygen isotope ratios are similar to IIE Fe meteorites. The possible primary parent body of H chondrites is the S type 6 Hebe asteroid (Gaffey and Gilbert 1998), where a smaller source object was possibly ejected to another orbit closer to the sun, and H chondrites were chipped off from this source body. Other candidate parent bodies are 3 Juno and 7 Iris asteroids. H chondrites with increasing petrographic grade came from increasing depth of the parent body (Ganguly et al. 2013). Most H chondrites do not contain high P–T transformations. High P–T transformations were detected only in Suizhou (Chen et al. 2004) and Yamato-75100 (Tomioka and Kimura 2003) H6 chondrites, such as high-pressure polymorphs of olivine (wadsleyite and ringwoodite), low-Ca pyroxene (majorite, akimotoite, and perovskite phase), and plagioclase (hollandite phase). In other H chondrites, shock veins with silicate darkening of the clasts with melted matrix were observed but without high-pressure transformations.

Friedrich et al. (2014a) studied the Kernouvé H6 chondrite where the peak shock pressure did not exceed 21 GPa, and the primordial porosity was removed by impact-induced compaction, while the metal vein structures were formed by shock-induced shear deformation. Friedrich et al. (2014a) suggested the formation of the brecciated, cataclastic structure of the NWA7298 structure to be due to multiple impact events in the debris zone of the H chondritic parent body on S3–S4 of Stöffler's scale (Stöffler et al. 1991). Wittmann et al. (2010) studied LaPaz Ice Field clastic impact melts of meteorites, of which the metal-sulfide texture indicated impact temperatures between 950 and 1,500 °C and proposing the age of impact event years on the H chondritic parent body between 3,600 and 4,100 Ma.

Schmieder et al. (2016) suggested a rapid cooling rate of the surface of the H chondritic parent body (in the order of 10 °C/h) after impact events, according to their research on the Gao–Guenie H5 chondrite. In the Pultusk H chondrite, the deformation in silicate clasts and darkening of matrix in the cataclastite texture could have been caused by impact-induced frictional melting on the H chondritic parent body (Krzesińska et al. 2015).

Friedrich et al. (2017) introduced a new model for the implied source area of shocked meteorites on the parent body. Impact-induced deformation changes physical properties: reducing porosity, introducing foliation, compaction – reproducing porosity by brittle cracking of silicates (Sharp and DeCarli 2006). Brecciation effects can complicate interpretations as materials with different shock stages become mixed (Friedrich et al. 2014b, 2017): (1) the extent of post-shock annealing and (2) the ambient temperature of deformation. Post-shock annealing can potentially affect metal fabric and the olivine shock stage, but porosity should be much less affected by annealing.

Porosity is influenced by shock effects in a complex way: The elevated pre-shock temperature will decrease, lowering the chondrites' porosities and increasing foliation; multiple impacts will cause extra compaction and a decrease in porosity. The foliation rate and compaction increase with increasing shock stages.

The shocked meteorites can be grouped by influence of shock-porosity-foliation (SPF) character:

- Low SPF group (for low SPF) is any combination of post-shock annealing and elevated pre-shock temperature: annealing or high-temperature deformation on hot parent body. Shock melting is more characteristic in this group.
- Non-low-SPF chondrites produced on intermediate shock stages, porosities, and metal foliation on cold parent body; shock deformation was initiated at low temperatures and followed by rapid cooling.

Wide metal shock veins could have been produced by pre- or syn-metamorphic impact-related deformation of the preliminary intergranular porosity structure, due to incomplete compaction, which can occur in a crater. Such a feature is proposed to have been formed beneath the impact crater on the H chondritic body. Both high foliation and low porosity could have been enhanced, if a projectile collided with a warm parent body target (Friedrich et al. 2017).

Heterogeneously deformed olivine in the same meteorite could have been produced by inhomogeneous deformation due to localized shock pressure–temperature loading during shock wave propagation in non-uniform rocks (described in "Introduction").

The analyzed thin section (called "Csátalja crusted zone 002") was prepared with a thickness of 35 μm. The meteorite is highly shocked with up to 300-μm thick shock veins, chondrule fragments, and shocked mineral clasts. It is relatively transparent because its thickness is constant at around 30 μm, but the melted zones are of dark color.

The meteorite shows heterogeneous structure at cm scale, with eroded but still observable chondrules and heavily crushed, as well as melted units. These different spatial units suffered different degrees of shock-driven alteration.

Methodology

In this study, the analyzed thin section was prepared by Zsolt Kereszty, who had collected the sample. It is a 15×20 mm-sized, well-prepared thin section of almost constant thickness. During the analysis, these different methods were used and correlated: optical, X-ray, and IR.

For textural analysis and basic mineral determination, a Nikon Eclipse E600 POL polarization microscope was used with magnifications of 4, 10, 20, and 40 times. The elemental composition of certain sections of the sample was determined by 1–2 μm spatial resolution with electron probe microanalyzer (EPMA) on the sample covered with a vacuum-deposited thin, amorphous carbon layer, using a JEOL Superprobe 733 electron microprobe with INCA Energy 200 Oxford Instrument Energy Dispersive Spectrometer (HAS Research Centre for Astronomy and Earth Sciences, Institute of Geology and Geochemistry, Hungary). The analytical circumstances were 20 keV acceleration voltage, 6 nA beam current and count time of 60 s for the spot measurement, and 5 min for line scan analysis. Olivine, albite, plagioclase, and wollastonite were standards; we estimated the detection limit for main element identification below 0.5 wt% based on earlier measurements with various samples.

IR spectroscopy and microscopy were also applied to the sample. The attenuated total reflectance (ATR) method employed (Johnston and Premachandra 2001; Morlok et al. 2004; Chemtob et al. 2010; Udvardi et al. 2014; Kovács et al. 2015a) uses a crystal with a high refractive index in physical contact with the target (Ohta and Iwamoto 1985). The wave penetrates only a few μm below the surface as an evanescent wave and rapidly decays away from the interface. The reflected beam is attenuated with corresponding frequencies to the vibration mode and overtones of the sample crystals (Ferguson 2010). In this study, spectra were collected with a Bruker VERTEX 70 Fourier transform infrared spectrometer (FTIR) equipped with a HYPERION 2000 microscope with Bruker micro-ATR objective. To identify the region of interest in adjacent minerals, the ATR objective is used in the MCT-B visual mode. During the IR analysis, the minerals in the thin section were brought into contact with the tip of the germanium (Ge) crystal of 100 μm in diameter after the ATR objective was switched to the IR mode. With this approach, IR spectral information is gathered only from the surface layer of the sample to about 1/2 μm depth. The spatial resolution with 20× magnification was approximately 5–7 μm. All measurements were performed for 30 s (32 scans) at 4 cm^{-1} resolution. Bruker Optics' Opus 5.5. software was used for manipulation of the resultant spectra (e.g., ATR correction, baseline correction, atmospheric compensation, etc.).

Results

Petrography

Minerals on the meteorite

– *Olivine* is a major mineral occurring in 40% of the sample. It occurs in barred, porphyric and granular chondrules, also as megacryst in the matrix, in shock veins, and shock-induced melt pockets. Olivine has pink–blue–green interference color and straight extinction. All of the olivines in the shock veins and the melt pockets, and 30% of matrix-olivine, show mosaic extinction (Fig. 1). Olivine appears in hexagonal form in microgranular chondrules; whereas in porphyritic and granular chondrules, it occurs in tabular form as well as megacrysts. Olivines in the melt pockets and the shock veins are xenomorphous with resorbed rims. The size of the olivine grains varies between 5 and 200 μm; in recrystallized glassy chondrules, they are usually around 5 μm in diameter. Olivine clasts in shock veins and those in the melt pockets are 20–30 μm in size; whereas in chondrules, there are many 50- to 150-μm-diameter olivines.

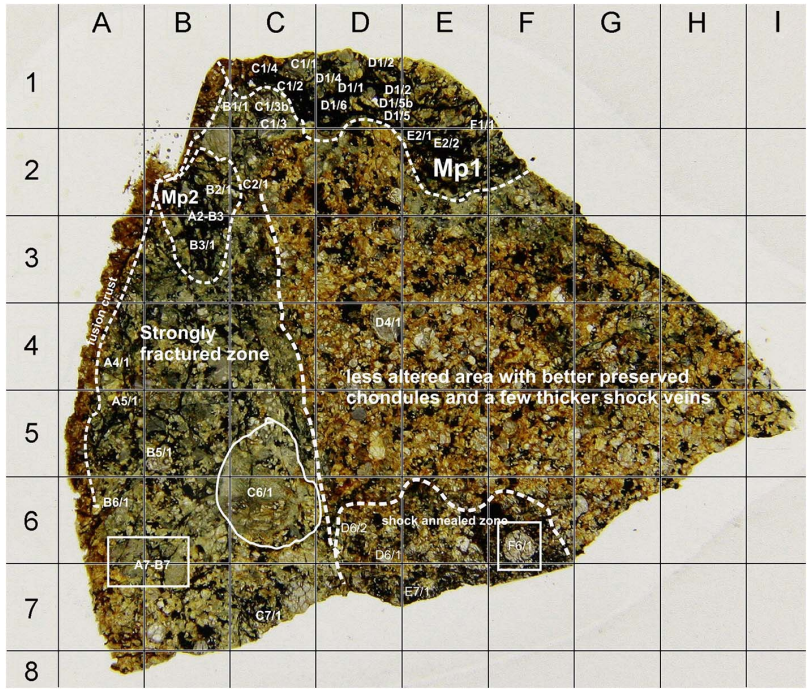

Fig. 1
Kink band structure in olivine with mosaicism

The large olivine megacrysts and the olivine grains near to the vein wall are about 100–300 μm in size (here, the minerals were not fragmented as much as in the deeper part of the veins).

– *Pyroxene* is a major mineral occurring in 30% of the sample. Pyroxenes have oblique extinction with gray–yellow interference color; the granular chondrules have a columnar shape of 70–100 μm in size. Pyroxenes in shock vein and matrix are xenomorph-shaped and fragmented; in veins and melt pockets, they are 20–100 μm in size and have mosaic extinction with isotropic patches (1–5 μm in size; Fig. 2). These isotropic patches follow junctions of fractures. Their resorption rims preferentially occur on the side closer to the shock veins because of the more elevated temperature in that direction. The pyroxenes in the melt pockets annealed along the fractures and the sub-grain boundaries.
– *Opaque minerals (black in transmitted light in microscope)* make up 10–20 wt% of the sample. The 80 wt% of these opaque minerals are kamacite grains with high reflectance (bright white color) occurring as 300- to 500-μm-sized amoeboid patches. Near the shock veins the kamacite occurs in irregular but also rectangular form, following vein walls showing plessite structure (intersection of 3- to 5-μm thick tetrataenite lamellae), and as fine-grained material (as 1–10 μm sized globules) of shock veins. Magnetite (occurrence 8 wt%) shows gray

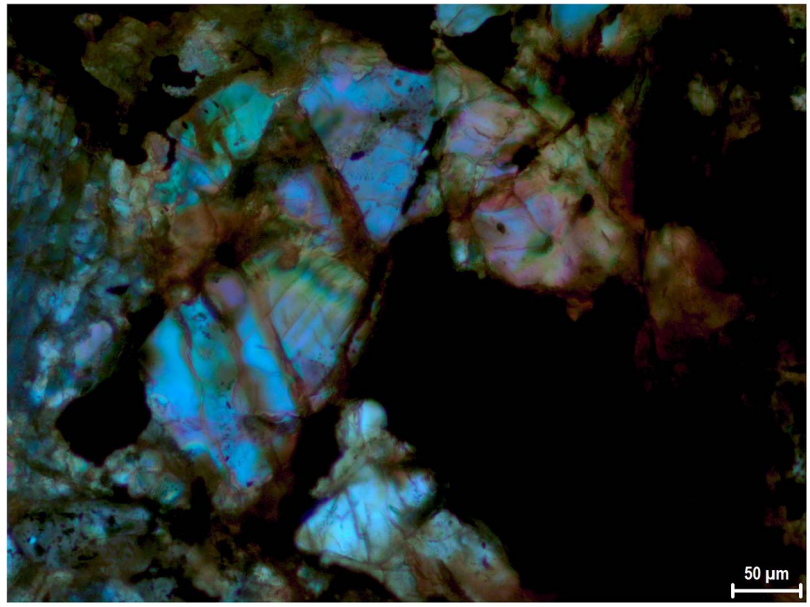

Fig. 2
Examples for the shock-produced structures in the meteorite. See details in the text. Labeling on the insets: ak – sub-grained shock-annealing structure in pyroxene, mgn – magnetite, pyr – pyrite, PF – planar feature, lam-aki – PF near shock-annealing structures (gray diffuse features in pyroxene)

reflectance color. At the lower part of the sample, large kamacite grains occur together with troilite. Troilite (occurrence 12 wt% of the opaque minerals) has an etched surface showing yellow–brown reflectance color and indicates miscibility with magnetite in the melt pocket. Magnetite occurs as numerous veins in the fusion crust (A3–A7) in 30-μm-sized thicker veins, crossed by a 3- to 5-μm-sized perpendicular, branching structure. At many locations, magnetite oxidized to Fe oxide. Among those veins in the fusion crust-layered structure, composed of magnetite and Fe oxide layers, some can be seen as 50- to 100-μm-sized units. Amoeboid magnetite patches were also observed in the fusion crust.

– On average 5% of the sample is composed of *Fe oxides* (*reddish, slightly transparent in transmitter light*). Around 90% of minerals of the meteorite are coated by Fe oxide staining in the entire sample. This staining appears as strewing, along the fractures, and as alteration product of opaque minerals. The upper part of the fusion crust (A3–A7), which is separated by a 30-μm thick magnetite vein from inner part, is filled with Fe-oxides, in higher spatial density than in the other parts of the sample.

Shock features. The shock features are introduced below: Microfaults are introduced as concept microtectonics, which feature latter was observed in shocked meteorites (Treiman 1995) and impact metamorphic rocks (Ferrière 2008). These features were observed in the cataclastic zone of our Csátalja sample: part of chondrules moved from each other.

Shock veins are branching veins with a maximal thickness of 100 μm; the melt pocket is a large, irregularly shaped area with 200 μm–2 mm dimensions, which contain annealed clasts. Melt veins are dark silicate veins with a thickness of 10–50 μm, without occurrence of mineral clasts within, only μm-sized metal sulfide pebbles.

The lamellar deformation microtexture is a summary term for planar deformation (PDF textures), planar fractures (PFs; Fig. 2), and of the shock-induced kink bands (Fig. 1).

Sub-grains are crystal domains that are embedded in melt in the shock-annealed aggregate. Mosaicism is variation in extinction and in interference color in a mineral grain, which was caused by shock metamorphism.

Sub-granular structure is characteristic for all shocked olivines and pyroxenes. The sub-granular structure, in the case both olivines and pyroxenes, is composed of sub-grains varying 3–5 μm in size, and the sub-grained minerals always occur inside of the mineral melt in the melt pockets and the shock-annealed zone. The transformation of minerals to high-pressure phases is initiated at sub-granular structures (Sharp and DeCarli 2006).

Mosaicism: Those olivines, which showed strong mosaicism, could have disordered texture, because we did not obtain proper $(Fe, Mg)_2SiO_4$ composition, compared with chondrule olivines in less shocked parts.

The spatial change of grain-size distribution also shows the result of shock effect: in the central part of the shock veins, clast sizes were 10–30 μm, whereas at the wall of

the shock vein grain sizes were around 300–400 μm. Outside the shock veins, 400 μm and occasionally larger grains were also present. For example, the mineral fragments in melt pockets can be grouped into two size ranges: 20–80 μm (within) and 150–300 μm (outer part).

Kink bands (shock deformation microstructures in olivines) and resorption rims. The *kink bands* in olivine were observed in only one grain near the shock veins. The thickness of kink bands was 5 μm; they are separated from one another by 10 μm, and are perpendicular in orientation to the wall of the shock melt pocket (Fig. 1). Resorbed depressions at the minerals' edges can be seen especially in MP1 and MP2; less are also present at the lower part of the shock-annealed zone. *This resorption* could be observed both in olivines and pyroxenes due to the reaction between melt and mineral clasts. The resorption, fragmentation, and number of fractures in the case of sub-grained pyroxenes are much more pervasive than in the case of other shocked pyroxenes.

For comparison, it is also important to analyze the characteristics of the less shocked area (Fig. 3). It contains well-preserved chondrules which are not fragmented; all of them, however, are crossed by Fe oxide veins varying 5–15 μm in width. Differing from the MP1–MP2 zones, here, the opaque minerals appear as large aggregates, which are less altered. This less shocked area is crossed by a few shock veins (thickness between 30–70 μm), which have shocked pyroxene and olivine clasts showing mosaicism in the dark matrix in transmitted light, without resorption rim and fragmentation in the veins. In this less shocked area, the shock deformation micro-structures are not observed in mineral fragments of the veins.

Deformation microstructures were preserved in the wall of the large melt packet as PFs in the pyroxenes, and kink bands in the olivines. Lamellar deformation micro-structures are relatively rare in the sample. Here, the twins in pyroxenes show wavy isotropic appearance because of post-shock melting. Micro-deformation structures, mostly PFs, were observed in mineral clasts in the shock veins, at the boundary of fusion crust and inner part of sample.

Shock-deformed and shock-produced minerals. The opaque minerals are also deformed and melted due to shock metamorphism: the kamacites show plessite texture and troilite shows lamellar miscibility with magnetite. Mosaicism occurs both in case of pyroxenes and olivine.

Pentlandites were identified in melt pockets in the vicinity of pyrites and kamacite grains; sometimes, the globules are in metal-silicate immiscible pentlandite melts with a size range of 3–7 μm, and are composed of kamacite and troilite. The pentlandite occurrences were determined by electron microprobe measurements; their diameter varied between 10 and 100 μm, where magnetite appeared as an alteration rim. The *opaque minerals* ware also deformed and melted due to shock metamorphism: the kamacites show plessite texture; troilites show lamellar miscibility with magnetite.

Pyroxene shock deformation toward shock annealing started from the outer part of those pyroxenes, which are close to shock melt and to weakness zones, such as fractures, PFs, and PDFs – although it is difficult to determine whether a given location

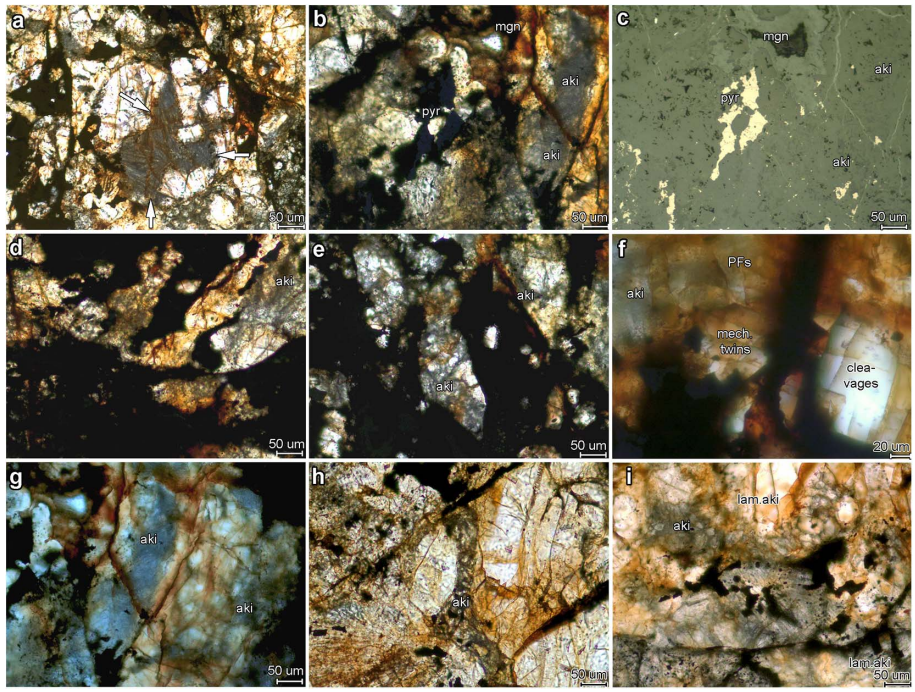

Fig. 3
Overview of the analyzed thin section, with the main areas: MP1 (top), MP2 (top left), shock-annealed zone (bottom), fusion crust (left), shock-fractured zone (middle left)

definitely reached the phase of being mixed shock melt. The transformation preferentially occurs at the sub-grain boundaries of pyroxenes. Around 30% of all large (100–150 μm) pyroxene grains that are located close to shock veins are altered in this way, whereas the alteration rate in the case of tiny (10–50 μm) pyroxenes reaches 50%–70%. Overall, about 30% part of each large pyroxene clasts are transformed toward shock melt.

Structural units in the studied meteorite

Based on optical microscope analysis, the following main units were identified in the sample (Fig. 3): Two large melt pocket areas (MP1: C1–F3 zones, MP2: B2–B3 zones, where MP is for melt pocket), fusion crust (A3–A6 zone, separated by a magnetite-filled thick and long vein from the strongly fractured zone), shock-fractured area (B3–C6 zone), shock-annealed area (D6–F6 zone, also called "lower part"), and less shocked chondrule-rich area (all the rest, inside C2–F2–J5–D6 zone). We also use the term "upper part" (MP1 + MP2 and nearby surroundings) in the description.

In the general analysis of minerals in the meteorite, we already put more emphasis on shock-related features below (Fig. 3).

Melt pockets. The thin section contains differently shocked parts. The area C1–E1; E2–F2 (*MP1*) is a large shock vein, which is composed of minerals and chondrule fragments embedded in shock melt. The width of the large melt pocket varies between 1 and 4.5 mm, and it is 8-mm long. The second melt pocket is located at area B2–B3, which is 3-mm long and 1-mm wide. These two melt pockets have curved, embayed rims, and more parallel sub-veins can be observed (D1–E1). Frictional melting and shock wave propagation played roles in the formation of large melt pockets, based on shock wave experiments of Sharp and DeCarli (2006). Both melted areas contain shock-altered phases: tiny, 10- to 20-μm-sized sub-grained olivines are embedded in mineral melts and tiny pyroxene clasts below 80 μm in size show grayish cellular structure from shock annealing; the pyroxene sub-grains contain feldspar melt along the sub-grain boundaries. However, the large clasts are transformed only in 30% of their total area to grayish-cellular structure along the perimeters and fractures. Along the perimeter of the D1 clast, the shock melting of pyroxene is processed along the sub-grain boundaries, and shocked pyroxene shows cellular-like sub-grained (grain size is 1 μm or submicroscopic) dense structure along fractures (D1 area where akim3–4 IR were selected). Some shocked pyroxenes contain PFs (B2–B3: MP2), which were filled by dark shock melt. Chondrules in large melt veins occur near the wall of the shock veins, which are fractured, and the pyroxenes contain shock melt along the sub-grain boundaries and fractures. The olivine clasts in large melt pockets are lamellar, fractured, including isotropic patches and showing strong mosaicism. The dark part of the melt pockets consists of kamacite, and mineral melt including kamacite and troilite globules. The metal-sulfide globule-bearing (5- to 10-μm-sized kamacite–troilite globules) mineral melt is located in a 100- to 600-μm-long area near shock-annealed pyroxenes. The large kamacite grains (300–500 μm) show plessite exsolution by taenite, and troilite shows 10-μm thick exsolution bands with magnetite. The kamacites usually begin to alter to magnetite along 10- to 200-μm thick rims, which show zonation in reflected light (plessite structure).

The largest melt pocket (MP1) contains a few larger chondrules of pyroxene with radial and granular texture, which contain numerous fractures that are filled by Fe oxide or shocked pyroxene. These chondrule remnants have resorbed rims and are sized around 800–1,000 μm. The shock fractured area contains numerous faulted chondrules with barred, radial, and granular texture.

Fractured area including shock veins. The second unit, the strongly fractured zone, is a rectangular area from A3–C3 (except for the melt pocket MP2 mentioned above) to A7–C7. This area is composed of 100- to 300-μm thick major shock veins, which split up to 2–3 sub-veins. The opaque minerals, mostly kamacite, occur along the walls of the shock veins. The chondrules in this zone are strongly fragmented (B6-1 and B5-1), and moved along the microfault in the shock veins. Between the shock veins, amoeboid kamacite assemblages occur in a size range of 100–500 μm, but

these kamacites show no exsolution with taenite or alteration, in spite of the large melt pockets. This area shows only clastic deformation; no high-pressure phases were observed microscopically. This area contains a large recrystallized composite chondrule (C6-1), which is crossed by shock veins and perpendicular shearing zones. Shock annealing is relatively rare but a 20-μm thick vein of the A51 granular chondrule contains dark shock melt. Darkening of the silicate clasts were observed in this area.

Shock-annealed area. This area is located in the D6–F6 – D7–F7 rectangle, which is a shock-heated area, where the olivines show brown staining, and a 100 μm part of the D62 olivine chondrule is altered to shock-annealed sub-grained structure. The black area is composed of kamacite and mineral melt. This area contains only two chondrules, and the melt pocket contains mostly large (100–150 μm) shock-annealed mineral fragments that float in melt. A large megacryst was observed in this area (D6-2). The opaque assemblages, which are composed of kamacite and troilite (E7-1), contain pyroxene and olivine inclusions.

This area contains fragmented, but not faulted and shifted, chondrules of 500–1,000 μm in size with radial, granular, and porphyritic textures. The shock-fractured chondrule contains a composite chondrule [composed of several individual chondrule fragments (C6/1 object in Fig. 3), which originally showed different chondrule texture types, confirming that these fragments were not produced by the shock event in the meteorite] with an area of 4.5 mm^2, including radial, porphyritic, and barred textures.

Less shocked, chondrule-rich area. The less shocked chondrule-rich unit (C2–D2, D3–G3, D4–G4, D5–G5) contains a lesser number of major shock veins with 100–150 μm thickness than other areas in this thin section (D3–G3 and E5–H4), which are filled by clasts. The clasts are olivines and pyroxenes showing strong mosaicism. The dark part of the vein consists of mineral melt. The chondrules, which are sheared by a shock vein, are fragmented and moved about 50 μm from each other by microfaults. This area is affected mostly by thermal metamorphism and has been less overprinted by shock metamorphism than other areas (MP1, MP2, shock-annealed zone, strongly fractured zone). The entire matrix is recrystallized and composed of large kamacite pockets (100–300 μm), of pyroxene, and of olivine with grain sizes of 50–80 μm. The chondrules were classified into two groups according to their size: (a) 100–200 and (b) 300–600 μm. The whole area is infiltrated by Fe oxides, which occur as numerous, 3- to 5-μm thin hematite-filled fractures and reddish-brown staining of silicates. The D41 chondrule has parquetted-like texture which could have been caused by rapid cooling of that chondrule where the needle-like crystallites show random orientation.

Elemental distribution of shock effects

Elemental compositions were affected by the shock effects in the studied sample. Measurements thereof are presented in the tables in detail: Table 1 shows

Table 1
Comparison of composition of shocked and non-shocked olivines and pyroxenes in the meteorite

	Non-shocked part				Shock vein and melt pocket			
Olivine								
wt%	Min	Max	Average	Deviation	Min	Max	Average	Deviation
SiO_2	43.7	47.2	44.7	1.85	40	45	43.2	1.83
FeO total	15.8	18.2	16.7	1.3	16.4	20.7	16.7	1.3
MnO	0	0.63	0.27	0.24	0	0.57	0.27	0.24
MgO	35.9	39.2	38.4	1.17	36.1	42.4	39	1.9
Pyroxene								
wt%	Min	Max	Average	Deviation	Min	Max	Average	Deviation
SiO_2	52	62.3	59.2	4.1	54.2	61.5	58.61	2.9
Al_2O_3	0	80.37	2.56	2.96	0	8.63	2.91	3.09
FeO total	50.29	14.7	9.9	2.8	6.2	11.6	8.93	1.73
MnO	0	00.51	0.06	0.18	0	0.61	0.19	0.29
MgO	12.9	27.4	21.6	5.7	10.25	27.15	20.09	7.12
CaO	00.54	18.62	5.45	5.57	0	17.6	8	7.8
Na_2O	0	20.8	0.95	1.05	0	2.94	0.71	1.13
Cr_2O_3	0	10.98	0.33	0.71	0	1.11	0.31	0.4

the comparison of shocked and non-shocked olivines and pyroxenes; Table 2 shows compositions of shock melt in pyroxenes; Table 3 shows the composition of opaque minerals around chondrules, whereas their shocked versions can be seen in Table 4.

Several observations point to element migration by shock annealing

– More Ca is present in the melt-vein *pyroxenes* than in other pyroxenes outside of melt veins, because with the shock alteration of the pyroxenes, Ca, Al, and Na *show increasing occurrence*. An example can be seen in the large, shocked, sub-granular pyroxene (Tables 1 and 2, Fig. 2) with sub-granular structure that contains shock melt alteration along a 50-μm thick fracture. The shocked host pyroxene has normal $FeMgSiO_3$ composition, but that part which was altered toward shock melting has elevated Ca, Al, and Na contents relative to the less altered part. Beside the above-mentioned elements, the occurrence of *Cr may also increase along with the shock effect.*

Table 2
Composition of the shock melt in pyroxenes in the sample

	Shock melt in pyroxene			
wt%	Min	Max	Average	Deviation
SiO_2	54.2	63.6	58.9	3.25
TiO_2	0	1.01	0.18	0.38
Al_2O_3	0	18.9	5.01	5.96
FeO total	2.28	11.6	8.00	2.69
MnO	0	0.62	0.14	0.27
MgO	1.67	27.0	17.3	8.82
CaO	0	17.6	8.47	7.39
Na_2O	0	7.88	1.59	2.60
K_2O	0	0.97	0.16	0.34
Cr_2O_3	0	1.11	0.31	0.40

The table contains measuring points numbered akim3−10 and ring1−2, where the akim1−2 points are shocked pyroxenes

Table 3
Composition of opaque minerals around chondrules in the non-shocked part of the meteorite

B2−C1	Opaque minerals around chondrules								
Zone mineral	Ap1 apatite	op1 mix	op3 pent	op4 kam	op2 mag	Min	Max	Average	Deviation
O	26.0	36.9	3.21	n.d.	31.5	3.21	36.9	24.4	14.8
Na	2.00	n.d.	n.d.	n.d.	n.d.	–	-	–	–
Mg	2.20	n.d.	n.d.	n.d.	n.d.	–	-	–	–
Si	0.72	4.36	0.41	n.d.	n.d.	0.41	4.36	1.83	2.20
P	20.0	0.38	n.d.	n.d.	n.d.	0.38	20.0	10.2	13.9
S	n.d.	n.d.	32.6	n.d.	n.d.	-	-	–	n.d.–
Ca	31.0	8.28	n.d.	n.d.	4.11	4.11	31.0	14.5	14.5
Fe	6.21	49.1	50.0	92.3	64.4	6.21	92.3	52.4	31.2
Ni	n.d.	0.99	9.02	6.32	n.d.	0.99	9.02	5.44	4.09

Table 4
Composition of shock-affected opaque minerals in melt pockets

Opaque minerals in shock melt pocket																						
	C1–D1													F1				Calculations				
Zone mineral	x1 mag	x2 tro	op10 pent	op11 tro +pent	op12 mix	op13 mix	x3 mag	op5 tro	op6 tro	op7 mag	op8 mag	op14 kam	op15 kam	op16 kam	op17 tro	op18 tro	op19 tro	Min	Max	Average	Deviation
O	28.5	n.d.	3.51	6.57	18.8	17.1	29.4	n.d.	n.d.	29.3	30.2	n.d.	n.d.	n.d.	n.d.	n.d.	5.22	3.51	30.2	18.7	11.3
Mg	n.d.	n.d.	n.d.	n.d.	n.d.	2.74	n.d.	n.d.	n.d.	n.d.	n.d.	n.d.	n.d.	n.d.	n.d.	n.d.	n.d.	2.74	2.74	2.74	
Al	n.d.	n.d.	n.d.	0.13	0.19	n.d.	n.d.	n.d.	n.d.	n.d.	n.d.	n.d.	n.d.	n.d.	n.d.	n.d.	n.d.	0.13	0.19	0.16	0.04
Si	n.d.	0.58	1.14	2.13	3.45	5.78	n.d.	n.d.	n.d.	7.22	n.d.	n.d.	n.d.	n.d.	n.d.	n.d.	1.30	0.58	7.22	3.09	2.54
P	n.d.	n.d.	n.d.	0.32	0.32	n.d.	n.d.	n.d.	n.d.	n.d.	n.d.	n.d.	n.d.	n.d.	n.d.	n.d.	n.d.	0.32	0.32	0.32	0
S	n.d.	35.3	29.7	26.1	14.1	9.04	0.76	35.8	35.8	n.d.	n.d.	n.d.	n.d.	13.8	35.9	35.1	31.9	0.76	35.9	25.3	12.5
Fe	71.5	60.9	35.5	37.4	35.3	32.0	65.8	62.6	64.1	60.1	69.8	92.3	92.0	87.0	63.9	62.7	59.9	32.0	92.3	61.9	18.6
Ni	n.d.	1.03	25.9	18.6	15.2	8.99	2.64	n.d.	n.d.	3.41	n.d.	5.42	5.72	1.79	n.d.	n.d.	n.d.	1.03	25.9	8.86	8.34
Cu	n.d.	n.d.	n.d.	n.d.	n.d.	n.d.	1.45	n.d.	n.d.	n.d.	n.d.	n.d.	n.d.	n.d.	n.d.	n.d.	n.d.	1.45	1.45	1.45	

- Beside the variation in certain elements, their standard deviations also changed occasionally. In the pyroxenes, the standard deviations increased for SiO_2, MgO, and CaO abundance, in spite of the trend in the olivines along with the increasing shock effect. During the transformation from pyroxene toward the shock melt the standard deviation is decreased for SiO_2 and Fe total, while for Al_2O_3, CaO, and Na_2O the standard deviation increased.
- Ti behaves in a unique manner; it could be identified only in the case of the akim5 and akim10 spots, while K was identified in akim7 and ring2, suggestive of melting, as feldspars surrounding the small pyroxene sub-grains there.
- Along with the increasing shock effects in *olivines* the Fe content increased, MgO increased slightly, and Ca diminished in shocked olivines. The standard deviation decreased by the shock effect in the case of Si, Mg, and Fe content.
- The shock melt along sub-grain structure has Ti and K content differing in the pyroxenes, which do not contain these elements, and they are strongly enriched in Ca, Al, and Na relatively to shocked pyroxenes. The shock melt along sub-grain structure in pyroxenes contains somewhat higher Cr content than the less shocked parts of pyroxenes. The Fe and Mn contents of shock melt along sub-grain structure decreased relatively to shocked pyroxenes.

The opaque minerals from the shock melt are characterized by the following mixed phases: kamacite + goethite, pentlandite + troilite, and relatively pure opaque minerals like pentlandite grains. Pentlandites have a 0.1–3.5 wt% O, Al, Si, and P, beside major elements in the shock melt, which could have been caused by diffusion from their vicinity due to shock annealing. Pentlandite and pyrite were found by energy dispersive X-ray spectroscopy (EDX) measurements; the data are correct. Pentlandite could have been formed primarily, but pyrite could be a secondary mineral (Csátalja was found in a marsh area, where pyrite easily could form as a secondary mineral). The pentlandite was found in shock melts and at the wall of shock veins; it occurs as a large amoeboid mineral in the chondritic area with troilite. The occurrence of troilite and magnetite in large opaque amoeboid mineral assemblages also could be due to weathering of kamacite. These grains show somewhat a chaotic appearance even with optical microscope. The mixed phases (like op13 in Table 4) are characterized by a few wt% Mg and Si. The opaque minerals around the pyroxene chondrule contain a few wt% Mg, Si, P, and Ca.

In Fig. 4, EPMA-based elemental distribution shows further examples of shock-annealing alteration of pyroxenes occurring together with elemental migration.

Element mapping. The element maps show moderate Ca–Al enrichment for the shock-annealed pyroxene ak7 (Fig. 4, 1st column; distorted sub-granular pyroxene EDX point) relative to host pyroxenes and to neighboring mosaic olivine. The Na enrichment can be observed only near EDX point akim5.

Near ak7 (Fig. 4A), EDX area hedenbergite was identified with IR spectroscopy. Near EDX point akim5 (Fig. 4, 1st column) several FTIR spectra were taken, which

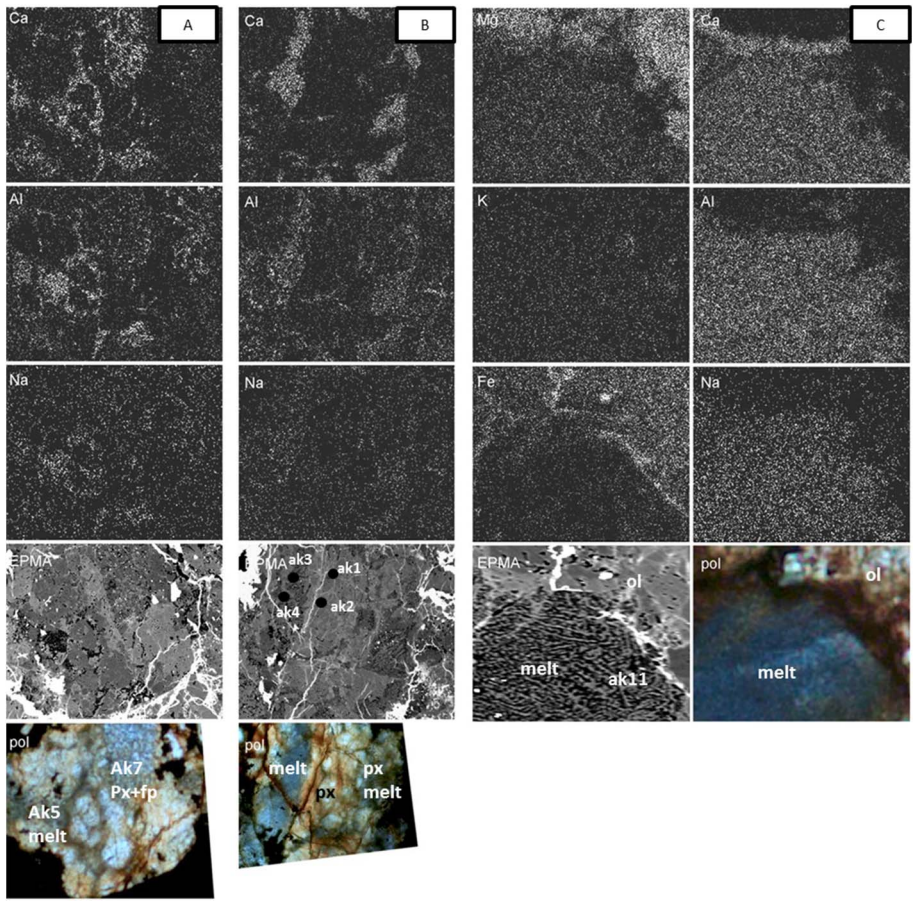

Fig. 4
Element mapping of shock-annealed pyroxenes (akim)

indicate presence of anorthite (major band at 950 cm^{-1} with shoulders of 875, 915 cm^{-1}, and band at 630 cm^{-1}).

D14 area (Fig. 4B). Moderate Ca and Al enrichment and minor Na enrichment can be observed in the shock-melted pyroxene. Two wide shock melt veins can be distinguished in the large D1 pyroxene clast: EDX points ak3 and ak4, and the area next to ak1–2 (gray area on microscope photo, "pol" inset). The akim3 point was well documented by IR spectroscopy. The ak1–3 IR spectra (Fig. 6) were taken near EDX points ak1–2–3 of the mineral melt of olivine and pyroxene composition (spectra composed of major bands of fayalite and minor additional bands of pyroxene).

D6 ak11 (Fig. 4C shock melt in pyroxene clast). The akim11 object (blue area in the lower right inset) does not show any differences in K to host olivine but does show depletion in Fe and Mg to host olivine. The BSE image of ak11 shows floating lath-shaped crystallites in dark matrix; the matrix has feldspar composition. The rim of the akim11 object shows moderate Fe and Ca enrichment, but a decrease of Al. The ak11 object shows strong enrichment of Ca, Na, and Al.

IR spectra of shocked minerals

We recorded the IR spectral profiles of several olivines and pyroxenes and correlated them with other shock-driven observations. For context comparison of different minerals' IR spectra are presented in Fig. 5 of poorly shocked minerals, corresponding peak positions can be seen in Table 5. The references of IR bands in Table 5 could not be fully accepted, because the IR bands are influenced by other features (the peak positions differ in ATR, transmittance, and reflectance mode), but in most cases, there is no better IR reference. Due to this problem, the reflectance and transmittance reference data should be used critically, which is stressed in the interpretation.

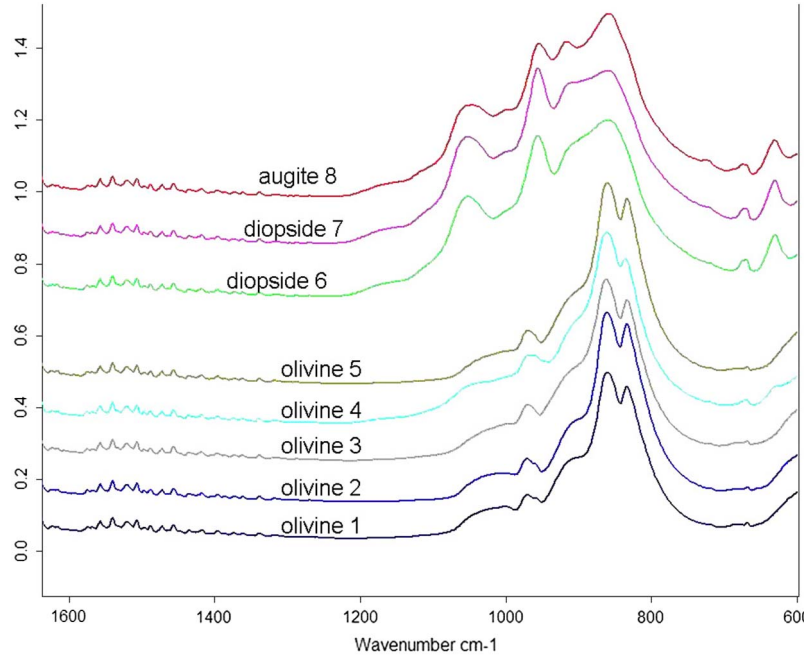

Fig. 5
Example of IR profiles for visualization of different peak positions

Table 5
Peak positions and their vibration types in pyroxenes and olivines using IR measurements

Mineral near to shock melt					Reference	
Peak position	Diopside (6–7)	Augite (8)	Shocked olivine (1–5)	Vibration type	Peak	Source
			605	Internal SiO_4 vibration	610	Hamilton (2010)
	630	635	628	Si–O deformation	633	Dyar et al. (2011), Jovanovski et al. (2009)
		660		Si–O deformation	670	Dyar et al. (2011), Jovanovski et al. (2009)
	670	675	673	Si–O deformation	670	Dyar et al. (2011), Jovanovski et al. (2009)
			830	Si–O symmetrical stretching	824–833	Morlok et al. (2006)
	855	851		Si–O–Si stretch vibration (non-bridge)	850 –1,100	Dyar et al. (2011), Jovanovski et al. (2009)
			860	Si–O bridge stretching	856–876	Hamilton (2010), Omori (1971)
			903	Mg^{2+}–Fe^{2+} in M2 position	929	Hamilton (2010)
	917	915		Si–O bridge stretching	920	Dyar et al. (2011), Omori (1971)
	955	955		Si–O–Si stretch vibration (non-bridge)	850 –1,100	Lane et al. (2011), Jovanovski et al. (2009)
			965, 970	Si–O antisymmetrical stretching	944–980	Hamilton (2010)
			1,020	Si–O–Si stretch vibration (non-bridge)	850 –1,100	Hamilton (2010), Jovanovski et al. (2009)
	1055	1053		Si–O–Si stretch vibration (non-bridge)	1057	Dyar et al. (2011); mixture of high and low Ca-px.

The numbers of measurement points in the 2nd, 3rd, and 4th columns correspond to the profiles in Fig. 4. The FTIR-ATR reference bands were added by Hamilton (2010) and Lane et al. (2011) for olivine and by Dyar et al. (2011). The additional information for vibration types are added by Jovanovski et al. (2009), Morlok et al. (2006), and Omori (1971)

Examples of unshocked *olivines* and pyroxenes can be seen in Fig. 5, demonstrating examples for the peak-based identification and analysis of minerals, and details can be found in Table 5.

The shock effect distorts the crystalline lattice of minerals, which is demonstrated in shifts of the peak positions of olivines in Fig. 6. The most intact olivine is spectrum A with the characteristic bands 837, 863, 923 sh (shoulder), 975 and 1,000 sh cm^{-1}. Spectra B and C are shocked fayalite, which contains pyroxene bands near 630, 670, 1,050, and 1,113 cm^{-1} from mixed structures.

The deformation of olivines shows the following features in Fig. 6:

- A: The measuring point akim1 is an olivine with the following bands: 837, 863, 923 sh, 975, and 1,000 sh cm^{-1}. This comes closest to intact olivine structure.
- B: Point akim2 shows additional bands beside the above-mentioned peaks (with more intensity): 641, 668, 687, 724, (743), 839w (weak peak), 861, 921, 973, 1,000, 1,043, and 1,100 sh cm^{-1} (the additional bands below 839 cm^{-1} and above 1,000 cm^{-1} belong to pyroxene; hence, this measuring point is proposed

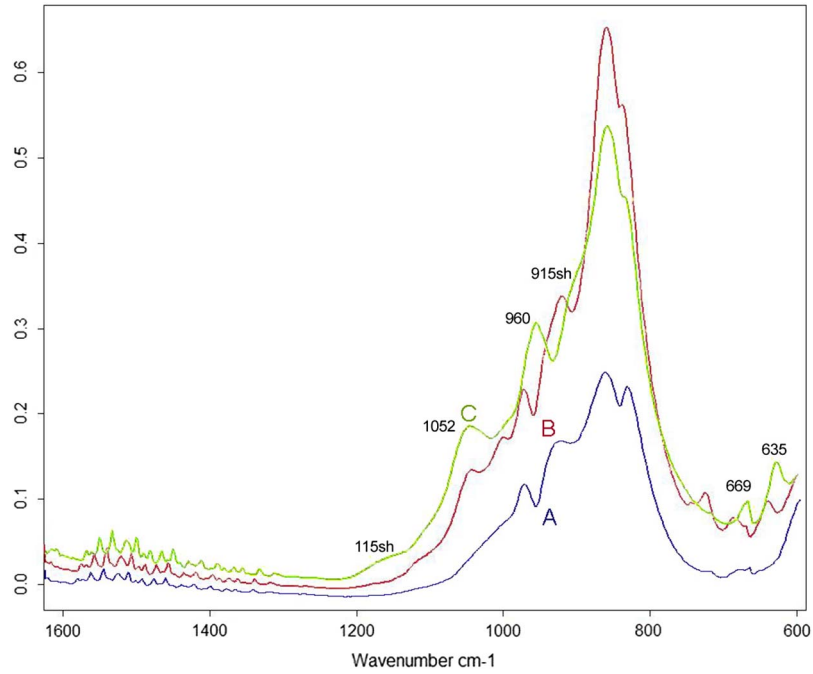

Fig. 6
Examples for the mixed structured minerals, with mainly olivine but also pyroxene peaks. The IR spectrum A is normal olivine, but spectra B and C contain forward pyroxene bands due to distortion of olivine because of shock loading. The pyroxene bands occur at 635, 669, 915 sh, 960, 1,052, and 1,115 sh cm^{-1}

to be at the boundary of fayalite and pyroxene by mixed mineral phase with olivine structure, but pyroxene composition: this measured grain could be a disordered fayalite.

– C: Point akim3 is characterized by weaker olivine, and stronger pyroxene peaks, together with additional peaks (635, 669, 838 sh, 862, 915 sh, 960, 1,052, and 1,115 sh cm^{-1}).

Discussion

In this section, we summarize and discuss the possible consequences and realization of shock-related effects, focusing on the structural changes in pyroxenes and their identification.

Shock-related processes

Impact-induced deformation changes physical properties: by reducing porosity, introducing foliation, and compaction – reproducing porosity by brittle cracking of silicates and fracturing. Brecciation effects can complicate the interpretations of materials with different shock stages, since they become mixed: (1) the extent of post-shock annealing (MP1 and MP2 in our sample from Csátalja) and (2) the ambient temperature of deformation (fractured zone in the Csátalja sample). Post-shock annealing can potentially affect metal fabric and olivine shock stage, but porosity should be much less affected by annealing. The brecciation is caused by shock compression.

Substantial spatial heterogeneity could be observed in the sample regarding the consequences of the shock effects. Shock stage classification was introduced by Stöffler et al. (1991). We use that system with modifications by Sharp and DeCarli (2006). In the most mechanically fractured (B3–C7) zone, shock melting is not dominant, while fractures have the highest spatial density, producing sheared chondrules, where silicate darkening occurs in both the matrix and the shock-annealed clasts. In the internal zone of the shock veins, smaller grain size is characteristic, probably produced mostly by melting and not only fracturing, suggesting the dominant presence of resorbed rims. The mineral fragments in the MP1 large melt pocket can be grouped into two size ranges: 20–80 μm (inner part) and 150–300 μm (outer part). The metal and melt, due to the viscosity aspects, moved to the walls of the fracture when accelerated by the shock pressure gradient. They were able to enclose only smaller silicate clasts. All pyroxenes inside the shock veins were at least partly altered, especially along the sub-granular edges. *Lamellar deformed microstructures* are relatively rare in the sample, because most of deformed minerals were melted by the high shock temperature.

The less shocked olivines and pyroxenes are displayed in Fig. 4 where olivine and pyroxene spectra could be well distinguished from each other. The major

doublet of olivine does not show shift from references. The minor band of the M2 cation position of the MgO–FeO octahedral shifted to a lower wave number, which could have been caused by shock-induced disordering. The less shocked pyroxenes nowhere show peak shift. The stronger shocked minerals show mixed composition of olivine and pyroxene (Fig. 5), with the appearance of a forbidden peak at 1,100–1,115 cm^{-1}, which does not occur in normal pyroxenes and olivines.

The shock metamorphic processes were different not only between structural units of the sample but also at mineral level. The shock melt occurred in the veins of the strongly fractured zone and in the melt pockets (MP1 and MP2). The melt pockets were formed by collapse of more parallel shock veins. Shock melting occurred along the sub-grain boundaries and fractures, which was identified by optical microscopy and element mapping. The shock melts were enriched in Ca, Na, and Al compared with their surroundings. According to our IR measurements, the dark shock melt contains a mixed olivine–pyroxene composition. The standard deviation decreases in the vicinity of melt pockets because the compositions are influenced by the melt, causing homogenization in compositions.

The interaction of shock waves with cracks and pores could have produced localized pressure and temperature heterogeneity, which were observed as shock-annealed clasts in shock-melt vein and as melt pockets, which formed by collapsing of the former parallel shock veins. The shock wave initially propagates along open cracks, producing melt veins along the former cracks because of shock collision-induced shearing. This produces heat after the passage of the wave. A key issue for the use of melt-vein assemblages for constraining shock pressure is the relationship between crystallization pressure and shock pressure. Thermal modeling of melt-vein quench shows that a 1-mm-wide melt vein requires hundreds of milliseconds to crystallize (Xie et al. 2001, 2003, 2006, 2011), whereas transient pressure heterogeneities equilibrate in about 1 μs for a sample with a 1-mm grain size. Therefore, nearly all the melt-vein crystallization occurs after pressure equilibration (Sharp and DeCarli 2006). Thus, the crystallization assemblages in a given melt vein will depend on the time required for melt-vein quench versus the duration of high shock pressures (Sharp and DeCarli 2006):

1. If the shock duration was longer than the crystallization time of the melt vein, crystallization would have occurred during high shock pressure and therefore have recorded the continuum shock pressure. High-pressure transformation has only been locally observed in the sample; the Na- and Ca-bearing rgt1 grain could be identified as jadeite, implying a peak shock stage of 17 GPa at 1,200 °C.
2. If the shock duration was roughly the same as that of the melt-vein crystallization, then melt-vein crystallization would record both the continuum shock pressure and a lower pressure of partial release; thus, the core of the vein might contain an assemblage that crystallized at a lower pressure than that of the rest of

the vein (Bencsik et al. 2013). This phenomenon is true for the MP1–MP2 melt pockets and for the shock-annealed zone.

3. If the shock pulse was shorter than the melt-vein quench time, crystallization of low-pressure assemblages in the core of the melt vein occurs (Bencsik et al. 2013). This phenomenon is true for the fusion crust and for the strongly fractured zone.

The *following shock-driven alteration features* were observed in the meteorite, indicating the corresponding temperature and pressure values:

– Cataclasitic texture (faulted chondrules, irregular olivine–pyroxene fragments, strong mosaicism, and deformation microstructures, such as PFs and mechanical twins) were found along vein walls (mostly in the MP1 and the MP2), and inside the shock veins at the strongly fractured zone, suggesting 10–15 GPa and temperature below 1,000 °C (Sharp and DeCarli 2006). Such alterations make up around 10%–20% of the sample. The cataclastic structure is characteristic for the strongly fractured zone. The dark shock veins, according to experiments of Bogert et al. (2003), could have developed under small shock pressure regime within low shock pressures, due to frictional shearing. Some dark, thick veins contain only olivines with undulatory extinction and irregular fracturing, and chromite in plagioclase melt form during high-temperature (1,600 °C) frictional melting, rather than due to high shock pressure regime temperature (Bogert et al. 2003). The high-temperature frictional melting with low shock pressure could have been formed due to low-angle impact event of projectiles (Pierazzo and Melosh 2000). The frictional, melting-shear/melting-induced cataclastic texture with metal-sulfide globules and melted matrix does not contain high-pressure minerals in most cases [Allen (H4, S2) and Kernouvé (H6, S1) meteorites], whereas in other cases, the black veins could contain a high number of shock features [Rose Hill (H5, S6) chondrite; Bogert et al. 2003]. Such dark melts occur in the fragmented zone and in melt pockets in our Csátalja sample. According to Tomkins (2009), the metal-troilite textures in shock veins are more likely formed by post-shock metamorphism, with a temperature 850 °C, which was described from thick glass veins of the Chergach H5 brecciated chondrite. The metal-troilite textures occur in melt pockets and in thick shock veins in the fragmented zone of the Csátalja sample. Metal-sulfide melt migration could also have been caused by impact-induced melting (Tomkins et al. 2013); isolated melt pockets (like MP2 in the Csátalja sample) could have been formed from shock stage S3–S4 (e.g., Gao–Guenie H5 chondrite). Krzesińska et al. (2015) described syn-impact-related, shear tectonic-induced frictional melting, and formation of cataclasitic features in the Pultusk H chondrite. They proposed formation of this texture by shock compression through a single impact event (such a cataclastic texture occurred in the fractured zone of the Csátalja sample). According to Ruzicka et al. (2015), the metal-sulfide globules accumulated in a zone with higher shear stress, which could have been formed within a

temperature range of 400–650 °C on the parent body (melt pockets, thick veins in the fractured zone of the Csátalja sample). In summary, frictional melting and shock wave propagation played a role in the formation of large melt pockets, which caused silicate darkening and the formation of dark shock veins, based upon shock wave experiments of Sharp and DeCarli (2006). Cataclasitic texture could have been formed by shock compression in a single impact event (Krzesińska et al. 2015).

- Sub-grained pyroxenes were observed in melt pockets, which contain troilite–kamacite globules and lamellar structured kamacite and troilite assemblages, suggestive of a pressure of 15 GPa and a temperature of 988 °C (MP1, MP2, inside the shock veins in the shock-annealed zone). At the rgt1 point, jadeite has been detected, indicating 17 GPa/1,200 °C at the peak shock stage in the shock-annealed zone. Comparing the IR spectra of shocked and non-shocked minerals, the unshocked doublets of olivine at 830 and 860 cm^{-1} were shifted to a higher wave number with increasing shock stages, which were observed previously by Raman methods (similar to olivines, the peak position of the pyroxenes shifts to higher wave numbers with increasing shock stage).
- The resorbed rim by shock melting is more common in pyroxenes than in olivines. The large melt pockets (MP1–MP2) show curved walls, possibly by superpositions of more shock waves near 1,000 °C and below 15 GPa (Sharp and DeCarli 2006). This phenomenon occurred in the large melt pockets and in part of the shock-annealed zone (DE7 and F6).
- Characteristic grain-size production was observed in the melt pockets, where the fragmentation produced smaller grains in the central regions of the melt pockets. The shock-fractured area could have been produced by localized melting due to compressive stress-driven adiabatic shearing of shock waves (Grady 1980). Compressional fractures could have formed during the exaction stage of impact crater formation (Grieve et al. 1977).

Element migration from shock effects

Because of the shock effects, elemental differences emerged between the minerals at different locations. The spatial inhomogeneities in SiO_2, MgO, and FeO could have been caused by post-shock annealing (Chen et al. 2004). In *olivine*, along with the increased shock annealing, Ca is depleted and went into the melt (in agreement with Treiman et al. 2007), just like Al and Na (Sharp and DeCarli 2006). The shock melt-vein olivines are characterized by higher fayalite content, where Fe could migrate from neighboring kamacite–pyrite assemblages and from metal globules in shock melts. In the shock-effected *pyroxenes*, the crystal lattice deformation during shock annealing allowed the incorporation of more Al, Ca, Ti, and K; also, Mg replaced Fe. Thus, Fe is depleted in shocked pyroxenes. The increased Ti content suggests high-temperature formation (Hawkesworth et al. 1984). Ti enrichment occurs during crystallization over 1,000 °C in terrestrial magmatic rocks (Hawkesworth et al. 1984).

The original Ca, Al, and Na could have been enriched in the melt, according to Walton and Shaw (2009). The shock melt is rich in S, Al, Ca, and Na, as these are incompatible elements; while Fe, Mg, and Cr depletion in shocked pyroxenes could also be observed, compared with the rest of the meteorite, in agreement with our observations.

An element trend could only be observed in those chondrules and their fragments which are located in the melt veins, demonstrating the effect of shock and melt on element mobilization. Here, the perimeter of chondrules shows elevated Ca content. This enrichment is caused by preferential melting and mobilization of Ca from plagioclase. The shock melt pockets and veins show mineral melts formed by shock impedance contrast, caused by spatial inhomogeneities and the presence of opaque minerals, giving rise to reflection and refraction of shock waves (Stöffler et al. 1991).

Conclusions

Analyzing shock-driven alterations in the recently found Csátalja meteorite, characteristic similarities could be identified in the shock-driven *alteration of olivines and pyroxenes*, like mosaicism and more rarely kink bands. Roughly with the same shock effect (in grains very close to each other) that produces mosaicism in pyroxene, sub-granular texture, and resorption edges appear for olivines and pyroxenes, but in both cases, only in the MP1 and the MP2 melt pockets.

According to Sharp and DeCarli (2006), generally, the melt-vein assemblages correspond to crystallization over a wide range of pressures from less than 3 GPa (La Landa and Kunishack meteorites) to approximately 25 GPa for the S6 samples (Sharp and DeCarli 2006). High post-shock temperatures have annealed out shock-metamorphic features and transformed high-pressure minerals back to their low-pressure polymorphs, nearly completely annealing shock features in ordinary chondrites that had been previously heavily shocked (Rubin 2004).

Compositional changes by element migration from shock effect in pyroxenes were also observed and confirmed that the melt was enriched in Si, Mg, Fe, Ca, Na, and Al. The shock effects elevated Ca and Al occurrence in the pyroxenes along with the progressing shock melting. It is also possible that such glassy pyroxenes with elevated Ca and Al occurrence might have left behind the retrograde transformation of akimotoite to pyroxene glass grains (Sharp and DeCarli 2006; Treiman et al. 2007; Ferroir et al. 2008). Ti and K appeared only in shocked pyroxenes because of incorporation into the crystal structure due to high shock temperature above 1,100 °C.

Resorbed features were characteristic only in melt pockets together with mosaicism and lamellar microstructure (15 GPa/1,000 °C in the MP1–MP2 melt pockets and the shock-annealed zone), while in shock veins fragmentation was dominant for both olivines and pyroxenes (10–15 GPa in the strongly fractured zone).

Because IR *ATR-based spectra characterization of shocked olivines and pyroxenes* are poorly published in the literature, we present these observations as a reference for future work. In general, olivine is characterized by IR bands near 830, 860, and 960–980 cm^{-1} and broad band near 1,000–1,020 cm^{-1}. Mosaic olivines show 635, 720, and 1,045–1,055 cm^{-1} bands. The less shocked pyroxene shows 630, 670, 720, 870, 920, 950, and 1,050 cm^{-1}. The shock-annealed pyroxene grains also show 630, 670, and 720 cm^{-1} bands, but there are new features as well: the shoulders at 840 cm^{-1} and the peak at 865 cm^{-1}. The pyroxene band 920 was shifted to 917 cm^{-1}, the band of 950 cm^{-1} split into bands of 940 and 958 cm^{-1}, and there appeared a new band of 1,000 cm^{-1}. The 1,050 cm^{-1} peak of pyroxene shifted to 1,043 cm^{-1} in the case of shock melting. The broadening of peaks and the shifting of the peak position to lower wave numbers indicate a crystal lattice defect. The occurrence of new forbidden bands indicates dimerization of olivine and pyroxenes, and distortion of the SiO_4 tetrahedra.

Acknowledgements

The authors are grateful to the HAS Research Centre for Astronomy and Earth Sciences for providing instrumental background, and to referees for advice in shock history and to Dr. Henry M. Lieberman for editing of the manuscript, and Dr. István Kovács for advice in part of the FTIR-ATR spectroscopy. The research was supported by the COST TD1308 project and the GINOP-2.3.2-15-2016-00003 grant.

References

Bencsik, A., K. Fintor, S.Z. Nagy, E. Pál-Molnár, I. Gyollai 2013: Short pressure pulse originated shock-veins in NWA-4983 S4 stage ordinary chondrite. – Meteoritics and Planetary Science, 48/S1, p. A54.

Bérczi, S.Z. 2000: Kis atlasz a Naprendszerről, 1.: Planetáris és anyagtérképek a holdkőzetekről, meteoritekről (Little Atlas of the Solar System, Part I: Planetary and Material Maps of Lunar Rocks and Meteorites). – Uniconstant, Budapest, 24 p. (in Hungarian)

Bérczi, S.Z., S. Józsa, Z.S. Kovács, B. Lukács, G.Y. Szakmány 2004: Studies of thermal evolution of chondritic asteroidal body: Synthesis from Antarctic meteorite thin section set of the National Institute of Polar Research, Tokyo. – Acta Mineralogica-Petrographica, 45/2, pp. 55–60.

Bogert, C.V.D., P.H. Schultz, J.G. Spray 2003: Impact-induced frictional melting in ordinary chondrites: A mechanism for deformation, darkening, and vein formation. – Meteoritics and Planetary Science, 38/10, pp. 1521–1531.

Chemtob, S.M., B.L. Jolliff, G.R. Rossman, J.M. Eiler, R.E. Arvidson 2010: Silica coatings in the Ka'u Desert, Hawaii, a Mars analog terrain: A micromorphological, spectral, chemical, and isotopic study. – Journal of Geophysical Research, Planets, 115/E4, p. E04001.

Chen, M., X. Xie, A.E. Goresy 2004: A shock-produced (Mg, Fe)SiO_3 glass in the Suizhou meteorite. – Meteoritics and Planetary Science, 39/11, pp. 1797–1808.

Dyar, M.D., T.D. Glotch, M.D. Lane, B. Wopenka, J.M. Tucker, S.J. Seaman, G.J. Marchand, R. Klima, T. Hiroi, J.L. Bishop, C. Pieters 2011: Spectroscopy of Yamato 984028. – Polar Science, 4/4, pp. 530–549.

Ferguson, P. 2010: Attenuated total reflectance – Fourier transform infrared spectroscopy analysis of pulsed electron deposited silicon dioxide film on silicon substrate. – Doctoral dissertation, Texas State University, San Marcos, TX, 75 p.

Ferrière, L. 2008: Shock metamorphism and geochemistry of impactites from the Bosumtwi impact structure. – Dissertation, University of Vienna, Vienna, Austria, 218 p.

Ferroir, T., P. Beck, B. Van de Moortèle, M. Bohn, B. Reynard, A. Simionovici, A. El Goresy, P. Gillet 2008: Akimotoite in the Tenham meteorite: Crystal chemistry and high-pressure transformation mechanisms. – Earth and Planetary Science Letters, 275/1, pp. 26–31.

Friedrich, J.M., J.C. Bridges, M.S. Wang, M.E. Lipschutz 2004: Chemical studies of L chondrites. VI: Variations with petrographic type and shock-loading among equilibrated falls. – Geochimica et Cosmochimica Acta, 68/13, pp. 2889–2904.

Friedrich, J.M., M.K. Weisberg, M.L. Rivers 2014a: Multiple impact events recorded in the NWA 7298 H chondrite breccia and the dynamical evolution of an ordinary chondrite asteroid. – Earth and Planetary Science Letters, 394, pp. 13–19.

Friedrich, J.M., G.C. Perrotta, M. Kimura 2014b: Compositions, geochemistry, and shock histories of recrystallized LL chondrites. – Geochimica et Cosmochimica Acta, 139, pp. 83–97.

Friedrich, J.M., A. Ruzicka, R.J. Macke, J.O. Thostenson, R.A. Rudolph, M.L. Rivers, D.S. Ebel 2017: Relationships among physical properties as indicators of high temperature deformation or post-shock thermal annealing in ordinary chondrites. – Geochimica et Cosmochimica Acta, 203, pp. 157–174.

Gaffey, M.J., S.L. Gilbert 1998: Asteroid 6 Hebe: The probable parent body of the H-type ordinary chondrites and the IIE iron meteorites. – Meteoritics and Planetary Science, 33/6, pp. 1281–1295.

Ganguly, J., M. Tirone, S. Chakraborty, K. Domanik 2013: H-chondrite parent asteroid: A multistage cooling, fragmentation and re-accretion history constrained by thermometric studies, diffusion kinetic modeling and geochronological data. – Geochimica et Cosmochimica Acta, 105, pp. 206–220.

Grady, D.E. 1980: Shock deformation of brittle solids. – Journal of Geophysical Research: Solid Earth, 85/B2, pp. 913–924.

Grieve, R.A., M.R. Dence, P.B. Robertson 1977: Cratering processes – As interpreted from the occurrence of impact melts. – Proceedings of the Symposium on Planetary Cratering Mechanics, Pergamon Press Inc., New York, NY, pp. 791–814.

Hamilton, V.E. 2010: Thermal infrared (vibrational) spectroscopy of Mg–Fe olivines: A review and applications to determining the composition of planetary surfaces. – Chemie der Erde - Geochemistry, 70/1, pp. 7–33.

Hawkesworth, C.J., N.W. Rogers, P.W.C. van Calsteren, M.A. Menzies 1984: Mantle enrichment processes. – Nature, 311, pp. 331–335.

Johnston, C.T., G.S. Premachandra 2001: Polarized ATR-FTIR study of smectite in aqueous suspension. – Langmuir, 17/12, pp. 3712–3718.

Jovanovski, G., P. Makreski, B. Kaitner, B. Boev 2009: Silicate minerals from Macedonia. Complementary use of vibrational spectroscopy and X-ray powder diffraction for identification and detection purposes. – Croatica Chemica Acta, 82/2, pp. 363–386.

Keil, K., K. Bell, F. Jeffrey, D.T. Britt 1992: Reflection spectra of shocked ordinary chondrites and their relationship to asteroids. – Icarus, 98, pp. 43–53.

Kovács, I., B. Udvardi, G.Y. Falus, M. Földvári, T. Fancsik, P. Kónya, E. Bodor, J. Mihály, C. Németh, G. Czirják, A. Ősi, Z.S. Varga-Barna, H.P. Bhattoa, Z. Szekanecz, S. Turcza 2015a: Az ATR FTIR spektrometria gyakorlati alkalmazása néhány– elsősorban földtani– esettanulmány bemutatásával (Practical – Especially earth science – Applications of ATR FTIR spectrometry through some case studies). – Földtani Közlöny, 145/2, pp. 173–192. (in Hungarian)

Kovács, J., I. Sajó, Z. Márton, V. Jáger, T. Hegedüs, T. Berecz, T. Tóth, P. Gyenizse, P.A. Podobni 2015b: Csátalja, the largest H4–5 chondrite from Hungary. – Planetary and Space Science, 105, pp. 94–100.

Krzesińska, A., J. Fritz 2014: Weakly shocked and deformed CM microxenoliths in the Pultusk H chondrite. – Meteoritics and Planetary Science, 49, pp. 595–610.

Krzesińska, A., J. Gattacceca, J.M. Friedrich, P. Rochette 2015: Impact-related noncoaxial deformation in the Pułtusk H chondrite inferred from petrofabric analysis. – Meteoritics and Planetary Science, 50/3, pp. 401–417.

Lane, M.D., T.D. Glotch, M.D. Dyar, C.M. Pieters, R. Klima, T. Hiroi, J.L. Bishop, J. Sunshine 2011: Midinfrared spectroscopy of synthetic olivines: Thermal emission, specular and diffuse reflectance, and attenuated total reflectance studies of forsterite to fayalite. – Journal of Geophysical Research, Planets, 116/E8, E08010.

Lange, M.A., P. Lambert, T.J. Ahrens 1985: Shock effects on hydrous minerals and implications for carbonaceous meteorites. – Geochimica et Cosmochimica Acta, 49, pp. 1715–1726.

Morlok, A., G.C. Jones, M.M. Grady 2004: FT-IR micro-spectroscopy of fine-grained planetary materials: Further results. – 35th Lunar and Planetary Science Conference, Houston, TX, Abstract no. 1622.

Morlok, A., J. Bowey, M. Köhler, M.M. Grady 2006: FTIR 2–16 micron spectroscopy of micron-sized olivines from primitive meteorites. – Meteoritics and Planetary Science, 41/5, pp. 773–784.

Ohta, K., Iwamoto, R. 1985: Lower limit of the thickness of the measurable surface layer by Fourier transform infrared attenuated total reflection spectrometry. – Analytical Chemistry, 57/13, pp. 2491–2499.

Omori, K., 1971: Analysis of the infrared absorption spectrum of diopside. – American Mineralogist, 56, pp. 1607–1616.

Pierazzo, E., H.J. Melosh 2000: Hydrocode modeling of oblique impacts: The fate of the projectile. – Meteoritics and Planetary Science, 35/1, pp. 117–130.

Przylibski, T.A., A.S. Pilski, P.P. Zagozdzon, R. Kryza 2003: Petrology of the Baszkowka L5 chondrite: A record of surface-forming processes on the parent body. – Meteoritics and Planetary Science, 38, pp. 927–937.

Rubin, A.E. 2004: Postshock annealing and postannealing shock in equilibrated ordinary chondrites: Implications for the thermal and shock histories of chondritic asteroids. – Geochimica et Cosmochimica Acta, 68, pp. 673–689.

Rubin, A.E., W.F. Bottke 2009: On the origin of shocked and unshocked CM clasts in H-chondrite regolith breccias. – Meteoritics and Planetary Science, 44, pp. 701–724.

Ruzicka, A., R. Brown, J. Friedrich, M. Hutson, R. Hugo, M. Rivers 2015: Shock-induced mobilization of metal and sulfide in planetesimals: Evidence from the Buck Mountains 005 (L6 S4) dike-bearing chondrite. – American Mineralogist, 100/11–12, pp. 2725–2738.

Schmieder, M., D.A. Kring, T.D. Swindle, J.C. Bond, C.B. Moore 2016: The Gao–Guenie impact melt breccias – Sampling a rapidly cooled impact melt dike on an H chondrite asteroid? – Meteoritics and Planetary Science, 51/6, pp. 1022–1045.

Sharp, T.G., P.S. DeCarli 2006: Shock effects in meteorites. – In: Lauretta, D.S., H.Y. McSween Jr. (Eds): Metoeorites and Early Solar System II. University of Arizona Press, Tucson, pp. 653–677.

Stöffler, D., K. Keil, E. Scott 1991: Shock metamorphism of ordinary chondrites. – Geochimica et Cosmochimica Acta, 55, pp. 3845–3867.

Tomioka, N., M. Kimura 2003: The breakdown of diopside to Ca-rich majorite and glass in a shocked H chondrite. – Earth and Planetary Science Letters, 208/3, pp. 271–278.

Tomkins, A.G. 2009: What metal-troilite textures can tell us about post-impact metamorphism in chondrite meteorites. – Meteoritics and Planetary Science, 44/8, pp. 1133–1149.

Tomkins, A.G., R.F. Weinberg, B.F. Schaefer, A. Langendam 2013: Disequilibrium melting and melt migration driven by impacts: Implications for rapid planetesimal core formation. – Geochimica et Cosmochimica Acta, 100, pp. 41–59.

Treiman, A.H. 1995: A petrographic history of Martian meteorite ALH84001: Two shocks and an ancient age. – Meteoritics and Planetary Science, 30/3, pp. 294–302.

Treiman, A.H., M.D. Dyar, M. McCanta, S.K. Noble, C.M. Pieters 2007: Martian dunite NWA 2737: Petrographic constraints on geological history, shock events, and olivine color. – Journal of Geophysical Research, Planets, 112/4, E04002.

Udvardi, B., I. Kovács, P. Kónya, M. Földvári, J. Füri, F. Budai, G.Y. Falus, T. Fancsik, C.S. Szabó, Z. Szalai, J. Mihály 2014: Application of attenuated total reflectance Fourier transform infrared spectroscopy in the mineralogical study of a landslide area, Hungary. – Sedimentary Geology 313, pp. 1–14.

Van Schmus, W.R., J.A. Wood 1967: A chemical-petrologic classification for the chondritic meteorites. – Geochimica et Cosmochimica Acta, 31, pp. 747–765.

Walton, E.L., C.S. Shaw 2009: Understanding the textures and origin of shock melt pockets in Martian meteorites from petrographic studies, comparisons with terrestrial mantle xenoliths, and experimental studies. – Meteoritics and Planetary Science, 44/1, pp. 55–76.

Wittmann, A., T.D. Swindle, L.C. Cheek, E.A. Frank, D.A. Kring 2010: Impact cratering on the H chondrite parent asteroid. – Journal of Geophysical Research, Planets, 115/7, E07009.

Xie, X., M. Chen, C. Dai, A. El Goresy, P. Gillet 2001: A comparative study of naturally and experimentally shocked chondrites. – Earth and Planetary Science Letters, 187, pp. 345–356.

Xie, Z., T.G. Sharp, P.S. DeCarli 2003: Estimating shock pressures from high-pressure minerals in shock-induced melt veins of the chondrites. – 34th Lunar and Planetary Science Conference, Houston, TX, Abstract no. 1280.

Xie, Z., T.G. Sharp, P.S. DeCarli 2006: High-pressure phases in a shock-induced melt vein of the Tenham L6 chondrite: Constraints on shock pressure and duration. – Geochimica et Cosmochimica Acta, 70, pp. 504–515.

Xie, Z., T.G. Sharp, K. Leinenweber, P.S. DeCarli, P. Dera 2011: A new mineral with an olivine structure and pyroxene composition in the shock-induced melt veins of Tenham L6 chondrite. – American Mineralogist, 96, pp. 430–436.